



HAL
open science

The 6 February 2023 Türkiye Earthquake Sequence as Detected in the Ionosphere

B. Maletckii, E. Astafyeva, S. Sanchez, E. Kherani, E. de Paula

► **To cite this version:**

B. Maletckii, E. Astafyeva, S. Sanchez, E. Kherani, E. de Paula. The 6 February 2023 Türkiye Earthquake Sequence as Detected in the Ionosphere. *Journal of Geophysical Research Space Physics*, 2023, 128 (9), pp.e2023JA031663. 10.1029/2023JA031663 . hal-04248389

HAL Id: hal-04248389

<https://hal.science/hal-04248389>

Submitted on 18 Oct 2023

HAL is a multi-disciplinary open access archive for the deposit and dissemination of scientific research documents, whether they are published or not. The documents may come from teaching and research institutions in France or abroad, or from public or private research centers.

L'archive ouverte pluridisciplinaire **HAL**, est destinée au dépôt et à la diffusion de documents scientifiques de niveau recherche, publiés ou non, émanant des établissements d'enseignement et de recherche français ou étrangers, des laboratoires publics ou privés.



RESEARCH ARTICLE

10.1029/2023JA031663

The 6 February 2023 Türkiye Earthquake Sequence as Detected in the Ionosphere

B. Maletckii¹ , E. Astafyeva¹ , S. A. Sanchez² , E. A. Kherani² , and E. R. de Paula² 

¹Institut de Physique du Globe de Paris (IPGP), Université Paris Cité, CNRS UMR 7154, Paris, France, ²Instituto Nacional de Pesquisas Espaciais (INPE), São José dos Campos, Brazil

Key Points:

- By using Global Navigation Satellite Systems data, we analyze ionospheric total electron content (TEC) response to the Turkey earthquake sequences of 6 February 2023
- We detect strong ionospheric response to two Mw 7.5+ earthquakes and weaker signatures after three smaller aftershocks with Mw < 6.7
- The TEC response was the largest on the south-west from the epicentral areas for all earthquakes

Supporting Information:

Supporting Information may be found in the online version of this article.

Correspondence to:

B. Maletckii,
maletckii@ipgp.fr

Citation:

Maletckii, B., Astafyeva, E., Sanchez, S. A., Kherani, E. A., & de Paula, E. R. (2023). The 6 February 2023 Türkiye earthquake sequence as detected in the ionosphere. *Journal of Geophysical Research: Space Physics*, 128, e2023JA031663. <https://doi.org/10.1029/2023JA031663>

Received 10 MAY 2023

Accepted 22 AUG 2023

Author Contributions:

Conceptualization: B. Maletckii, E. Astafyeva

Formal analysis: B. Maletckii, E. Astafyeva, S. A. Sanchez, E. A. Kherani, E. R. de Paula

Funding acquisition: E. Astafyeva

Investigation: B. Maletckii, E. Astafyeva, S. A. Sanchez

Methodology: B. Maletckii, E. Astafyeva, S. A. Sanchez, E. A. Kherani, E. R. de Paula

Resources: E. Astafyeva

© 2023. The Authors.

This is an open access article under the terms of the [Creative Commons Attribution-NonCommercial-NoDerivs License](https://creativecommons.org/licenses/by-nc-nd/4.0/), which permits use and distribution in any medium, provided the original work is properly cited, the use is non-commercial and no modifications or adaptations are made.

Abstract On 6 February 2023, a series of large earthquakes struck Turkey and Northern Syria. The main earthquake of Mw 7.8 occurred at 01:17:34 UTC and was followed by the three notable (Mw > 5.5) aftershocks within the next 18 min. Then, ~9 hr later, the biggest aftershock with magnitude Mw 7.5 and a Mw 6.0 earthquake occurred to the north-east from the first main earthquake. In this work, we use data of ground-based Global Navigation Satellite Systems (GNSS) receivers in Turkey, Israel and Cyprus to analyze the ionospheric response to this series of earthquakes. We separate these events in two groups: the first sequence of earthquakes (at 01–02 UTC) and the second sequence (at 10–11 UTC). For the first sequence, we observe a clear N-shaped total electron content (TEC) response after the Mw 7.8 mainshock earthquake and Mw 6.7 aftershock, and a smaller TEC disturbance that is, most likely, caused by the Mw 5.6 earthquake. The latter is now the smallest earthquake detected by using ionospheric GNSS data. The co-seismic ionospheric disturbances (CSID) propagated from the epicentral area in the south-west direction with velocities of about 750–830 m/s. For the second sequence, we observed the response to the Mw 7.5 aftershock earthquake and the Mw 6.0 aftershock. The CSID propagated both to the south-west and the north-west to the epicentral area, with velocities of about 950–1,100 m/s.

1. Introduction

It is known that large earthquakes can generate acoustic and gravity waves that propagate upward through the atmosphere and ionosphere and produce co-seismic ionospheric disturbances, CSID (e.g., Afraimovich et al., 2001; Astafyeva, 2019; Bagiya et al., 2017; Calais & Minster, 1995; Heki, 2021; Heki & Ping, 2005; Liu et al., 2011; Meng et al., 2019; Rolland et al., 2013). The co-seismic ionospheric disturbances (CSID) are usually detected in the vicinity of an earthquake's epicenter starting from 7 min after the onset. Co-seismic perturbations are often N-shaped, and their velocity of propagation varies between ~600 and ~1,500 m/s (i.e., close to the sound speed at the ionosphere altitudes).

Nowadays, the detection of CSID in data of GNSS-derived ionospheric total electron content (TEC) is quite frequent. However, not all earthquakes would produce signatures in the ionosphere. As of today, only earthquakes with moment magnitudes Mw > 6.6–6.8 were proven to generate CSID (Cahyadi & Heki, 2015; Perevalova et al., 2014). Sanchez et al. (2022) claimed to have detected the ionospheric response to the Mw 6.4 Ridgecrest earthquake of 4 July 2019 in California. However, they were not able to clearly identify N-wave signatures after the earthquake. Therefore, so far, the Mw 6.6 Chuetsu-oki earthquake of July 2007 in Japan remains the smallest earthquake ever recorded in the ionosphere (Cahyadi & Heki, 2015).

On 6 February 2023, a series of large earthquakes shook Turkey and Northern Syria. Two of these events were characterized by a moment magnitude of over 7. The earthquakes left behind a death toll of over 50,000 people in Turkey and Syria, becoming one of the five deadliest earthquakes of the twenty-first century.

In this work, we use data of ground-based GNSS receivers in Turkey, Israel and Cyprus and we analyze the ionospheric response to these earthquakes. We detect strong ionospheric response to two Mw 7.5+ earthquakes, but also weaker signatures after three smaller aftershocks with Mw < 6.7.

2. Data and Methods

We use phase measurements from dual-frequency Global Navigation Satellite Systems (GNSS) receivers to estimate the ionospheric TEC. TEC is equal to the number of electrons along a line-of-sight (LOS) between a satellite and a receiver:

Software: B. Maletckii, E. Astafyeva, S. A. Sanchez, E. A. Kherani, E. R. de Paula
Supervision: E. Astafyeva
Validation: B. Maletckii, E. Astafyeva, E. A. Kherani, E. R. de Paula
Visualization: B. Maletckii, E. Astafyeva, S. A. Sanchez
Writing – original draft: B. Maletckii
Writing – review & editing: B. Maletckii, E. Astafyeva, S. A. Sanchez

$$\text{slant TEC}_{ij}(\text{phase}) = \frac{1}{A} \times \frac{f_i^2 f_j^2}{f_i^2 - f_j^2} \times (L_i \lambda_i - L_j \lambda_j) \quad (1)$$

where $A = 40.308 \text{ m}^3/\text{s}^2$, L_i and L_j are phase measurements, λ_i and λ_j are wavelengths at the two the given frequencies (e.g., f_1 and f_2 frequencies of Global Positioning System (GPS) are 1,575.42 and 1,227.60 MHz, respectively). The TEC is measured in TEC units (TECu), $1 \text{ TECu} = 10^{16} \text{ electrons/m}^2$.

We use the ionospheric thin shell approximation to calculate the spatial positions of ionospheric disturbances. The intersection points between the shell (at a fixed altitude H_{ion}), and the LOS are called ionospheric piercing points, and their projections on the ground are known as sub-ionospheric points. Here we take the H_{ion} close to the maximum ionization altitude hmF2 (320 and 270 km at 01:17 UT and 10:24 UT, respectively) obtained by the nearest ionosonde station AT138 (38.0E; 23.5N) and by the IRI-2016 empirical model (Bilitza et al., 2017).

To study the ionospheric signatures driven by the earthquakes, we analyze data of 62 ground-based 1-s GNSS-receivers located in Turkey, Israel, and Cyprus that is, within $\sim 1,200 \text{ km}$ away from the earthquakes' epicenters (Figure 1a). During the earthquakes, each receiver captured $\sim 10\text{--}20$ satellites (GPS, GLONASS, Galileo, Beidou) at a time, providing more than 350 piercing points to study the ionospheric response, which made spatial resolution to be $\sim 0.35 \times 10^{-3} \text{ IPPs/km}$ (Figure S1 in Supporting Information S1).

Previously, researchers used band-pass filters or polynomial fitting to extract CSID signatures from the TEC data series (Afraimovich et al., 2001, 2010; Calais & Minster, 1995; Heki & Ping, 2005; Liu et al., 2011; Meng et al., 2019). However, filtering changes the waveform, amplitude and spectral components of a signal (Maletckii et al., 2020). Here we use the TEC time derivative, which serves as a high-pass filter and removes the bias and trend caused by the satellite orbit motion. In addition, the $d\text{TEC}/dt$ approach does not modify the amplitude of CSID (Maletckii & Astafyeva, 2021a, 2021b, 2022). Further, we estimate CSID spatio-temporal parameters by applying a real-time compatible interferometric method called D1-GNSS-RT (Maletckii & Astafyeva, 2021a) and by calculating travel-time diagrams (TTD, Maletckii & Astafyeva, 2021a; Maletckii & Astafyeva, 2022). The D1-GNSS-RT method allows to estimate the horizontal propagation speed and the direction of propagation by comparing CSID arrival times and positions at GNSS receivers. To detect CSID, the “D1-GNSS-RT” method first analyses the TEC data series to find the local maximum value (LMV). Then, it computes the cross-correlation function for each pair of time series around the LMV to calculate the difference in arrivals of the disturbances. Finally, based on these time shifts and by using an interferometric approach, it estimates the horizontal velocities of CSID propagation.

The main disadvantage of the D1-GNSS-RT method is that it is not applicable to sparse GNSS networks. In such a case, the apparent horizontal velocity of CSID can be estimated from TTD (Maletckii & Astafyeva, 2021a, 2022). The automatic near-real-time (NRT) TTD fitting technique consists of two stages: (a) the first maximum “picker” and (b) the “fitter” based on these maxima. To select the maximum along with all $d\text{TEC}/dt$ values, we pick the values exceeding a standard deviation of the series and a threshold of 0.08 TECu. In the case of the multiple values in the 120-s windows, we chose the centered one in this window. We also remove outliers from the final list of maxima in the given series (values that can appear only with velocities exceeding 5 km/s).

One other drawback of the D1-GNSS-RT is that previously it only performed successfully when the amplitude of $d\text{TEC}/dt$ disturbances exceeded the noise level by a factor of 4 (Maletckii & Astafyeva, 2021a). In the case of the Turkey earthquake, the noise level was initially too high to automatically subtract CSID. Hence, an additional adjustment was made. We smoothed all TEC series by using a central moving average with a 25-s window. This allowed us to significantly reduce the noise level without significantly reducing the amplitude of the signal and to reach the necessary signal-to-noise threshold. It should be noted that such a simple adjustment can be applied in NRT since it does not require significant additional stacking of the data (only an extra 12 s as compared to the initial methods).

3. Results and Discussion

On 6 February 2023, a series of large earthquakes occurred in Turkey in the vicinity of the northern border of Syria. The main shock of moment magnitude M_w 7.8 struck at 01:17:34 UTC. According to the US Geological

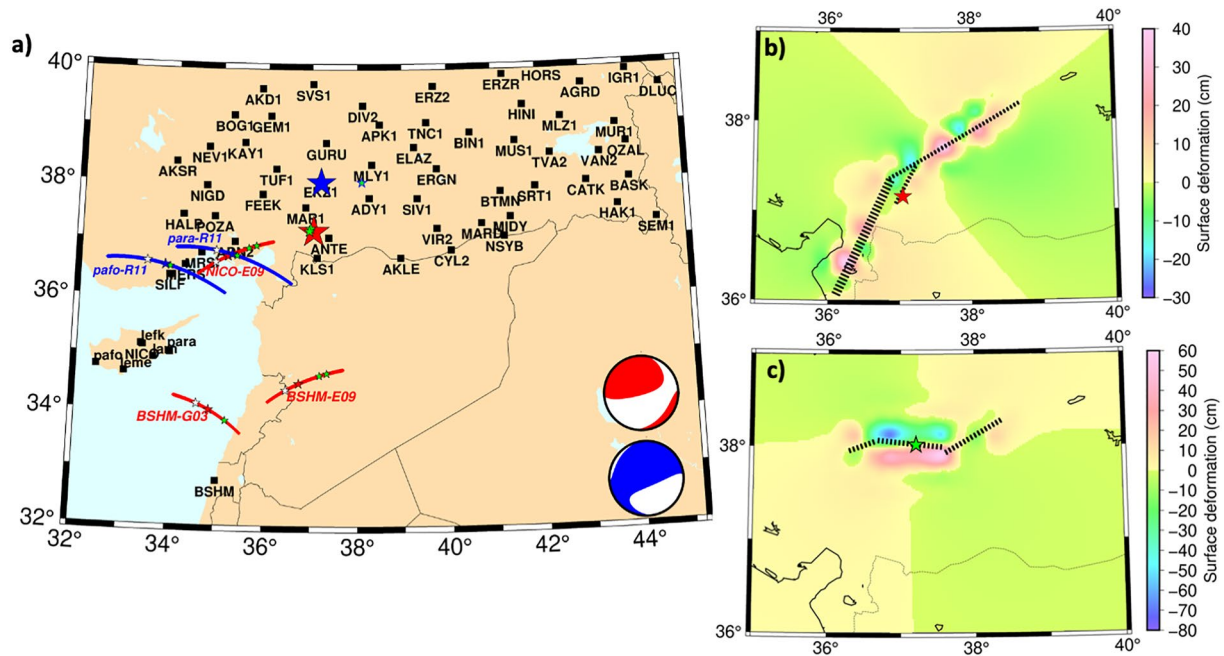


Figure 1. (a) Positions of Global Navigation Satellite Systems receivers (black squares), the earthquake epicenters (colored stars) and sub-ionospheric points (SIP) trajectories for the main total electron content observations. Red color relates to the Mw7.8 main shock, blue—to the major Mw 7.5 aftershock, green—to smaller magnitude aftershocks. White stars along the SIP traces show the earthquake onset time, red and blue stars show the detection position of co-seismic ionospheric disturbances (CSID) due to the main shocks, and small green stars indicate the position of CSID due to the aftershocks. (b) and (c) Surface deformations in vertical direction (in cm) occurred due to the main shock (b) and due to the major Mw7.5 aftershock (c), as estimated by the US Geological Survey. The corresponding color-scales are shown on the right.

Survey (The National Earthquake Information Center; <http://earthquake.usgs.gov>), the epicenter of this earthquake was located at 37.226°N and 37.014°E. The earthquake resulted from strike-slip faulting at a shallow depth (~10 km). According to preliminary estimates from finite-fault models, the major slip asperity is approximately 100 km long and 70 km wide (Figure 1). Despite the strike-slip focal mechanism, the vertical component of the surface deformation reached 40–50 cm (Figure 1b), which is a very significant number and is comparable to dip-slip earthquakes.

Within 18 min following the main shock, three moderate aftershocks occurred: Mw 5.7 at 01:26:50 UTC, Mw 6.7 at 01:28:15 UTC and Mw 5.6 at 01:36:27 UTC (Figure 2a). Because of their temporal closeness to one another, it was not possible to compute the focal mechanism for all aftershocks.

The biggest aftershock with magnitude Mw 7.5 occurred to the north-east of the first earthquake ~9 hr later, at 10:24:48 UTC. According to the USGS, the epicenter of this earthquake was located at 38.011°N 37.196°E. Initial estimates from finite-fault models point to a fairly small source, with the main slip asperity being only around 50 km long and 30 km wide. This earthquake was of strike-slip focal mechanism. However, it produced very significant displacements in the vertical plane: one can see subsidence down to 80 cm on the north from the epicenter, and an uplift of about 60 cm on the south from the epicenter (Figure 1c). This major aftershock was followed by the Mw 6.0 earthquake at 10:26:46 UTC (Figure 3a).

Below we analyze independently ionospheric response to the main shock and the 3 moderate aftershocks, and to the major Mw 7.5 aftershock and 6.0 aftershock, which we refer to as the first and the second earthquake sequences, respectively.

3.1. Ionospheric Response to the First Earthquake Sequence at 01–02 UTC

Figures 2b and 2c present ionospheric TEC and dTEC/dt time-series from stations “NICO” and “BSHM” and satellites G03 and E09. The first signature of CSID is seen at ~01:29 UTC, that is, 11.5 min after the main shock. It is N-shaped, with the depletion part lasting 9–10 min. Its amplitude is ~0.2–0.3 TECu.

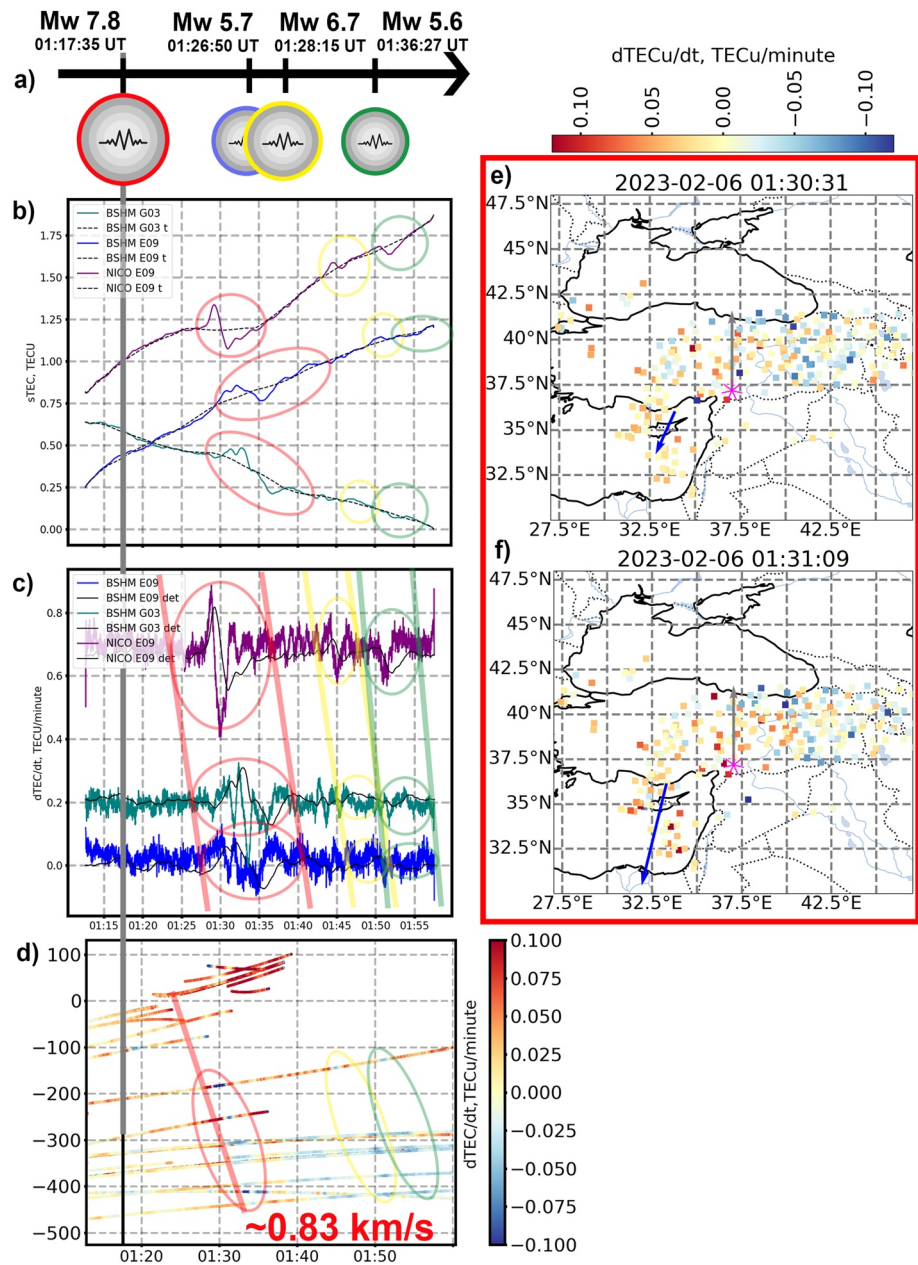


Figure 2. (a) The timeline of the first earthquake sequence at 01–02 UTC on 6 February 2023; (b) ionospheric total electron content (TEC) and (c) dTEC/dt time-series for stations “NICO” and “BSHM” and satellites G03 and E09. Each color circle corresponds to a specific earthquake from the timeline (a); The dashed line illustrates TEC trend (panel b, with index “t”) and detrended TEC data (panel c, with index “det”) (d) NRT-TTD by using data from “NICO,” “BSHM” and 5 receivers of the CYPOS Global Navigation Satellite Systems network using satellites G03, R04, E09. The source is placed at the location of the Mw. 7.8 Mainshock earthquake. The gray vertical line denotes the US Geological Survey onset time. Positive distances correspond to the values to the north of the earthquake epicenter, negative—south of the earthquake epicenter; (e) and (f) the first instantaneous velocities’ field obtained by the “D1-GNSS-RT.” dTEC/dt parameter presents as square colored dots. The gray arrow denotes the velocity vector of 1,000 m/s. The blue arrows correspond to the instantaneous velocities’ field of co-seismic ionospheric disturbances. The magenta star depicts the mainshock.

The second N-like CSID signature with an amplitude of ~ 0.1 – 0.15 TECu is observed at $\sim 01:45$ UTC. We consider this disturbance to be generated by the Mw 6.7 earthquake that took place at 01:28:15 UTC (37.189°N 36.893°E , 9.8 km depth). Furthermore, at $\sim 01:50$ UTC, we observed one more CSID signal of a duration of 2–3 min and an amplitude of about 0.08–0.1 TECu. Its waveform, however, differs from the classic N-like signature as we

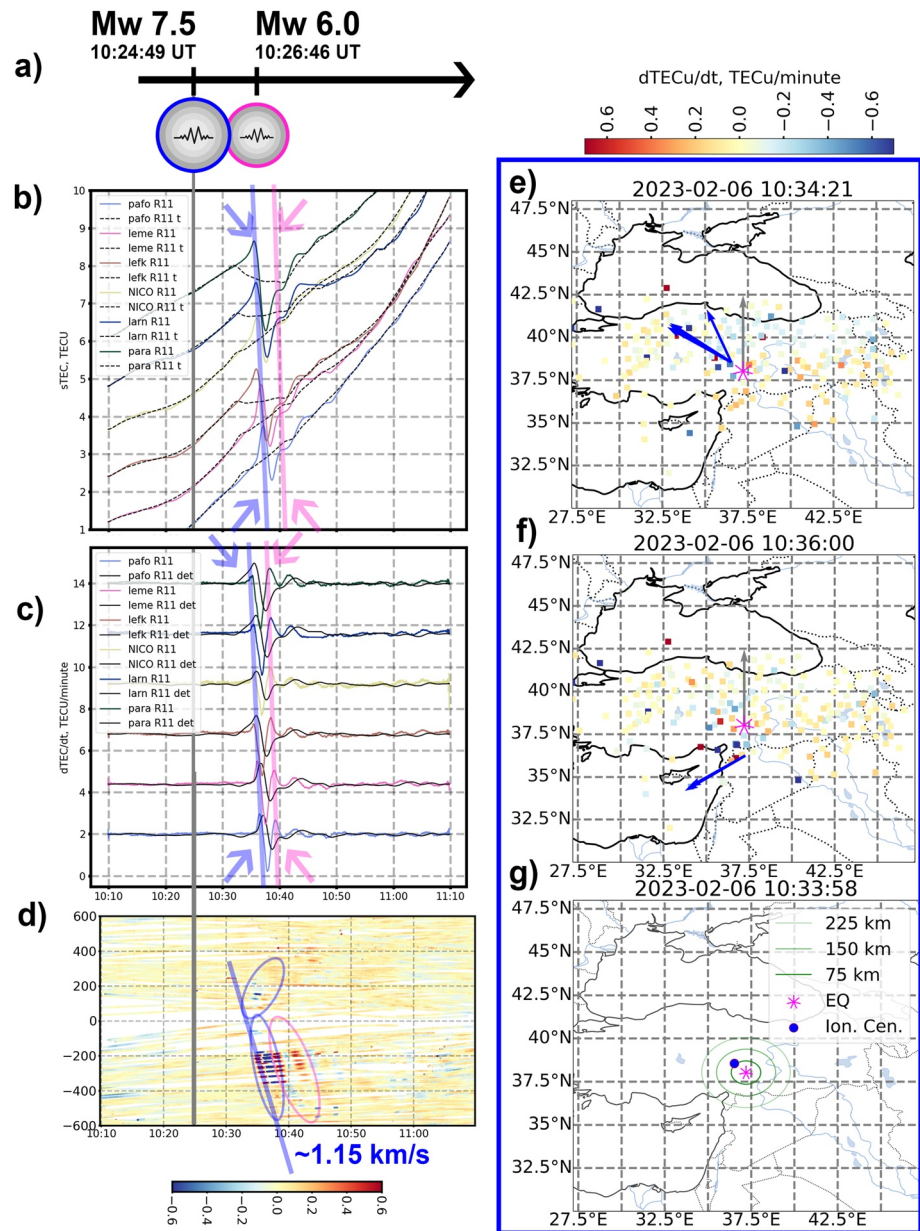


Figure 3. (a) The timeline of the second earthquake sequence at 10–11 UTC on 6 February 2023; (b) ionospheric total electron content (TEC) and (c) dTEC/dt time-series from station “BSHM,” the CYPOS network and satellites R11. Each color circle corresponds to a specific earthquake from the timeline (a); The dashed line illustrates TEC trend (panel b, with index “t”) and detrended TEC data (panel c, with index “det”) (d) NRT-TD by using data from “NICO,” “BSHM,” 5 receivers of the CYPOS Global Navigation Satellite Systems (GNSS) network and the TUSAGA-Aktif GNSS network using all satellites. The source is placed at the location of the major Mw 7.5 Aftershock earthquake. The gray vertical line denotes the US Geological Survey onset time; Positive distances correspond to the values to the north of the earthquake epicenter, negative—south of the earthquake epicenter; (e) and (f) the first instantaneous velocities’ field obtained by the “D1-GNSS-RT.” dTEC/dt parameter presents as square colored dots. The gray arrow denotes the velocity vector of 1,000 m/s. The blue arrows correspond to the instantaneous velocities’ field of co-seismic ionospheric disturbances. The magenta star depicts the Mw 7.5 major Aftershock. (g) The ionospheric source locations (blue circles) obtained from the instantaneous velocity vectors.

observe only a depletion that could be the negative phase of an N-wave (Figures 2b and 2c). Considering the time of observation and the waveform, we attribute this CSID to the Mw 5.6 aftershock earthquake that occurred at 01:36:27 UTC (36.992°N 36.683°E, 10.0 km depth).

These three disturbances can also be seen in TTD. Figure 2d shows NRT-TTD obtained by using data from “NICO,” “BSHM” GNSS stations and 5 receivers of the CYPOS GNSS network. The satellites used are G03, R04 and E09. One can see that the disturbances propagate southward away from the epicenter with an apparent velocity of about 0.826 km/s (the CSID due to the mainshock) and of about ~ 0.75 km/s (the response to the two aftershocks). We note that these velocity levels correspond to the sound speed values at ionospheric altitudes. Figures 2e and 2f show velocity estimations as obtained by the D1-GNSS-RT method for the CSID generated by the mainshock. Figure 2e shows the instantaneous velocity vector at 01:30:31 UTC, that is, 777 s after the earthquake onset time, on the south-west from the earthquake epicenter. The first horizontal velocities of the CSID obtained by the D1-GNSS-RT are 0.65 and 1.46 km/s.

3.2. Ionospheric Response to the Second Earthquake Sequence at 10–11 UTC

Figures 3b and 3c show the ionospheric TEC and dTEC/dt time series recorded after the major Mw 7.5 aftershock that occurred at $\sim 10:24$ UTC. Here we present data from station “BSHM,” the CYPOS network and satellite R11. The first signature of CSID appeared at $\sim 10:35$ UTC, that is, 11 min after the earthquake, and is characterized by the amplitude of ~ 2 TECu. It consists of two N-like waveforms. At $\sim 10:41$ UTC, we observed a new CSID signature in the TEC data series. We consider that this CSID was produced by the Mw 6.0 aftershock earthquake that occurred at $\sim 10:26$ UTC. This CSID is also characterized by the N-like waveform, its amplitude is about ~ 0.15 – 0.3 TECu and the duration is about 2–3 min.

Figure 3d shows 1-s TTD for all satellites and receivers (e.g., all LOS). From these data, the fitting method estimates the velocity to be 1.153 km/s. The TTD shows that the first signatures appeared both on the north and the south from the epicenter. However, then, the CSID mostly propagated southward.

Figures 3e and 3f show the results of the application of the D1-GNSS-RT method to the analysis of ionospheric TEC disturbances generated by the Mw 7.5 Aftershock Earthquake. The CSID velocity field maps for the first arrivals following the earthquake are shown in Figures 3e–3g, and the localization results are presented in Figure 3g. Figure 3e shows the first velocity vectors at 10:34:21 UTC, that is, 572 s after the earthquake onset time, at first on the north-east of the earthquake. The first horizontal velocities of the CSID are about ~ 950 – $1,100$ m/s, that is, they correspond to acoustic and shock-acoustic waves. The first velocity vectors are used to compute the first source location at the point with coordinates 38.548°N ; 36.528°E (Figure 3g) at 10:33:58 UTC. This time is consistent with the one obtained by NRT TTD. The subsequent CSID evolution after the next ~ 2 min changes the tendency for the direction of propagation, it starts to propagate in the south-west, while the velocities stay to be ~ 950 – $1,100$ m/s. This value agrees with our NRT-TTD fitting technique results and retrospective analysis (Haralambous et al., 2023; Vesnin et al., 2023).

3.3. Can Small Earthquakes Generate Visible N-Signatures?

Up to date, the 2007 Mw 6.6 Chuetsu-oki earthquake remains the smallest earthquake ever recorded in the ionosphere (Cahyadi & Heki, 2015), and, up to date, there were no observations of distinct N-like CSID signatures from an earthquake with a magnitude below 6.6. Here, for the first time, we detect clear N-shaped TEC variations that seem to be the response to earthquakes with magnitudes Mw 5.6 and 6.0. It should be emphasized that this finding is very unusual and requires additional reasoning in order to prove the link between the observed signatures and the small-magnitude earthquakes.

In both cases, the observed disturbances seem to be of an acoustic nature because, first of all, their apparent horizontal propagation velocity is about 750–950 m/s. Second, we observe the signatures ~ 10 min after the earthquake onset time (Table 1), which is in line with previous observations. Such timing is also in agreement with the time of the vertical propagation of acoustic waves from the ground to the ionosphere. The theoretical propagation time can be estimated from the sound speed profile calculated for the day, time and location of the earthquakes. The profiles for both events are calculated by using the empirical NRLMSISE-2 model (Emmert et al., 2020) and are shown in Figures S2a and S2b in Supporting Information S1. Based on the weighted average and the averaged values of the sound speed, during the first sequence, the acoustic waves take ~ 8.27 – 11.28 min (i.e., from 8 min 17 s to 11 min 17 s, respectively) to reach 320 km of altitude (i.e., the altitude of detection, $H_{\text{ion}} = 320$ km, Figure S2a in Supporting Information S1). For the second earthquake sequence, the time of the vertical propagation of acoustic waves up to the altitude of detection $H_{\text{ion}} = 270$ km (Figure S2b in Supporting Information S1) is ~ 9.42 – 10.07 min, that is, between 9 min 25 s and 10 min 4 s.

Table 1
Parameters of the 6 February 2023 Earthquakes and of the Corresponding Co-Seismic Ionospheric Disturbances (CSID)

Time (UTC)	Mw	Epi. location (Lat; Lon)	UT/Dist, km of the first CSID arrival	CSID source switch-on time on the ground, UT
01:17:34	7.8	37.226°N; 37.014°E	01:28:09/184 (NICO-E09)	01:16
			01:28:25/410 (BSHM-G03)	
			01:28:49/310 (BSHM-E09)	
01:28:15	6.7	37.189°N; 36.893°E	01:43:58/145 (NICO-E09)	01:30
			01:44:16/415 (BSHM-G03)	
			01:44:33/297 (BSHM-E09)	
01:36:27	5.6	36.992°N; 36.683°E	01:49:16/128 (NICO-E09) 01:49:38/291 (BSHM-E09)	01:35
10:24:48	7.5	38.008°N; 37.211°E	10:34:36/234 (para-R11)	10:24
			10:34:53/265 (NICO-R11)	
			10:34:50/262 (Iarn-R11)	
			10:35:47/352 (pafo-R11)	
10:26:45	6.0	38.032°N; 38.098°E	10:37:43/228 (para-R11)	10:27
			10:37:54/252 (NICO-R11)	
			10:37:59/256 (Iarn-R11)	
			10:38:48/346 (pafo-R11)	

Further, knowing the CSID detection time and the acoustic wave traveling time, we can estimate the time of CSID generation on the ground. For this purpose, we estimate so-called CSID onset time over the source, by using the NRT-TTD (Figure 2d) and by determining the time when the velocity slope line connects with 0 km of distance, which is 01:25:59 UTC. Therefore, the first CSID was generated at ~01:16 UTC. For the other two responses, the CSID onset times are: 01:40:00 and 01:44:43 UTC. Hence they were generated at ~01:30 and 01:35 UTC, which is very close to the onset times of the earthquakes (Table 1).

For the second sequence, the CSID onset time is 10:33:25 UTC. Therefore, the earthquake that could generate the first CSID occurred at ~10:24 UTC. For the second response, the CSID onset time is 10:36:29 UTC; hence, the time of the CSID source was at ~10:27 UTC. We note that the switch-on times of the CSID source on the ground are very close to the onset times for all earthquakes.

In addition, we perform a numerical modeling of the propagation of acoustic waves from the epicenter to the ionospheric altitudes for both earthquake sequences. For this purpose, we use the modeling tool that was previously used for the simulation of the ionospheric response to the propagation of tsunamis (Kherani et al., 2012) and that of seismic waves (Sanchez et al., 2022). Here, an N-wave pulse was launched from the epicenters at the times of the earthquake onsets in order to simulate the propagation of acoustic waves for both sequences of earthquakes (Text S1 in Supporting Information S1, Figure 4). The results are shown in Figure 5. One can see good agreement between observations and simulations for both earthquake sequences. Therefore, it is very likely that the small half-N-like disturbances are due to small-amplitude aftershocks.

Besides the above explanation, the observed CSID could also potentially have been a manifestation of gravity and acoustic-gravity waves due to the mainshock and due to the major Mw 7.5 aftershock, respectively. However, this scenario seems unlikely, because the gravity waves usually take about 30–60 min to reach the altitude of the ionosphere. Whereas we observe the response in 22 min (for the Mw 5.6 aftershock) and in 13 min (for the Mw 6.0 aftershock) after the earthquake time. Also, we have to note that gravity waves usually have quasi-periodic waveforms (e.g., Astafyeva, 2019), while here we observe N-like signatures.

Finally, the CSID observed between 01:28 and 01:49 UT (i.e., the first CSID sequence) could also be explained by a very extended fault of several hundreds of kilometers, and multiple significant uplift segments that occurred due to the mainshock (Figure 1b). The rupture lasted about 90–120 s, and the length of each of the major sub-faults was about 160–180 km (<https://earthquake.usgs.gov/earthquakes/eventpage/us6000jllz/finite-fault>).

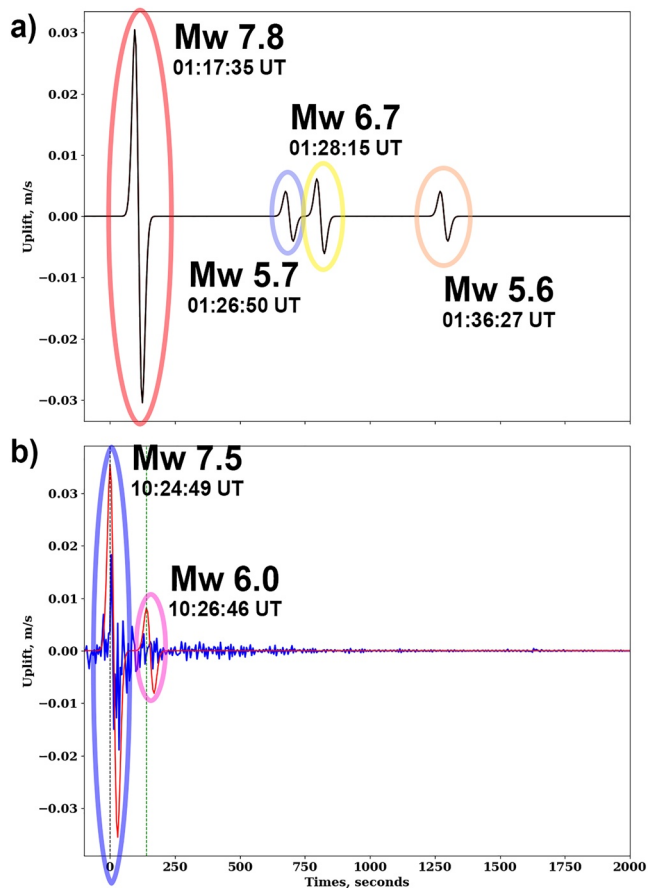


Figure 4. (a) The Gaussian N-like forcings used to simulate the ionospheric response to the Mw 7.8 mainshock (red circle) and aftershocks of Mw 5.7 (blue circle), Mw 6.7 (yellow circle), and Mw 5.6 (beige circle) used for modeling the total electron content (TEC) response of the first 01–02 UTC sequence; (b) the Gaussian N-like forcings (in red) used for simulation of the ionospheric response to the aftershocks with Mw 7.5 (blue circle), Mw 6.0 (rose circle) used for modeling the TEC response of the second 10–11 UTC sequence. The recorded ground motion from the seismometers around the epicenter is shown in blue for the second 10–11 UTC sequence.

Potentially, each of the segments can produce N-like disturbance, tens of seconds apart and several tens of kilometers apart. This would lead to the generation of a complex waveform signal, with multiple peaks. However, in such a case the peaks would be separated by a short interval of time, and this is what we clearly see for the first response at ~01:28 UT at LOS BSHM-E09 and NICO-E09 (Figure 3a), and what is proved by numerical experiments (Bagiya et al., 2023). While, the other two CSID are observed at 01:43 and 01:49 UTC, that is, 15 and 21 min after the first CSID, which is too long for the propagation of the acoustic waves. Therefore, this scenario does not seem credible.

In the case of the second earthquake sequence, the fault is much more compact (Figure 1c) and the rupture only lasted 40–60 s, but the uplift is more significant (<https://earthquake.usgs.gov/earthquakes/eventpage/us6000j1q4/finite-fault>). Since we observe the second signature only ~3 min after the first one, it is possible that it was caused by the same uplift region.

Future studies, especially modeling, will shed light on peculiarities of generation of ionospheric disturbances by small earthquakes.

3.4. CSID Amplitude and Propagation

In Figures 1–3, one can notice that the strongest ionospheric response was detected by GNSS receivers located in Cyprus and Israel (station BSHM, Figure 1a). While the majority of receivers in Turkey did not detect clear and visible CSID signatures in the ionospheric TEC. Such an “anisotropy” in the CSID amplitudes could be explained by several factors. First, this could be due to an anisotropic energy release during the earthquakes as was previously observed for other large earthquakes with long and large-dimension faults (e.g., Afraimovich et al., 2010). In the case of the first earthquake sequence, ground-based seismometer data showed that the rupture propagated westward (Melgar et al., 2023).

Second, both the waveform and the amplitude of the CSID largely depend on the conditions of observations, such as magnetic field configuration in the epicentral area, the geometry of GNSS-sounding and the background ionization (Astafyeva et al., 2014; Bagiya et al., 2017, 2019; Heki & Ping, 2005; Rolland et al., 2013). Near the epicenters of the Turkey earthquakes, the declination angle is ~55°, and the inclination is ~5°, so that one can expect the largest amplitudes on the south and southwest from the epicenter.

From the GNSS-sounding point of view, the satellite PRN E09 had the most favorable geometry for CSID observations (Figure 1a): the LOS senses the ionosphere on the south-west to the earthquake, and the disturbance mostly propagates in this direction as well. Hence, the clearest signatures are present in data obtained by the satellites E09, G03 (for the first sequence) and R11 (for the second sequence).

Last but not least, the amplitude of CSID depends on the magnitude of the initial forcing: larger earthquakes and larger co-seismic displacements generate larger disturbances in the ionosphere (Astafyeva et al., 2013, 2014; Cahyadi & Heki, 2015). In the case of the earthquakes under consideration, all of them seemed to be of strike-slip focal mechanism (e.g., <https://earthquake.usgs.gov>; CSEM-EMSC, 2023). Commonly, earthquakes with strike-slip faulting are characterized by large horizontal displacements and small vertical motion. However, in the case of the Turkey earthquakes, at least for the two major events, the vertical component of the co-seismic displacements was very significant and reached 40 cm during the mainshock and even 60 cm during the major 7.5 aftershock (Figures 1b and 1c). We consider that such strong displacements along with favorable geometry conditions allowed us to detect such a strong response at stations in Israel and Cyprus, that is, south-southwest from the epicenter.

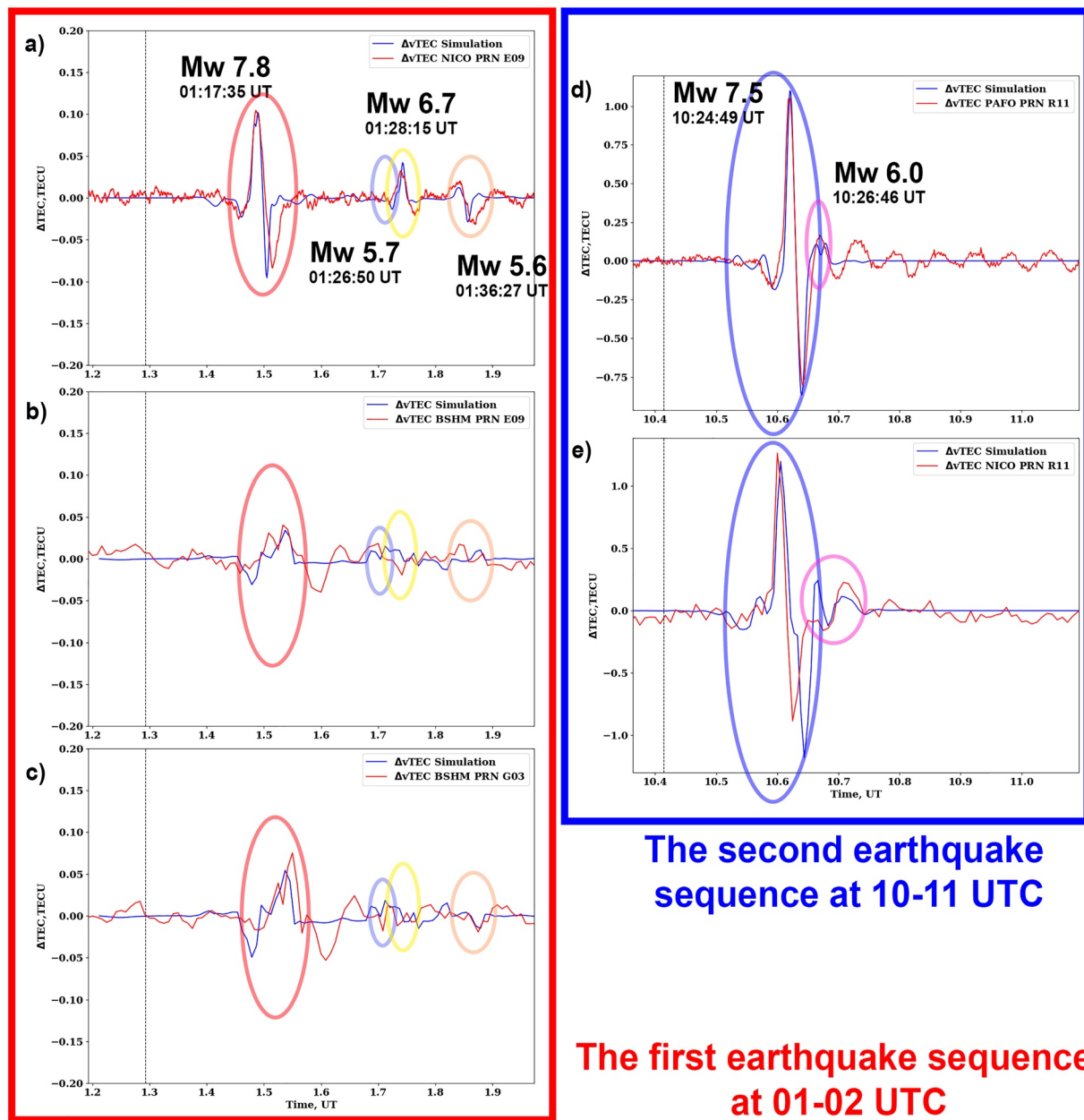


Figure 5. The comparison between simulated (blue curves) and observed (red curves) dvTEC based on the data from stations: (a) “NICO” (satellite E09), (b) “BSHM” (satellite G03), and (c) “BSHM” (satellite G03) within 35 min from the mainshock onset time, (d) “pafo” (satellite R11) and (e) “NICO” (satellite R11) within 35 min from the Mw 7.5 aftershock onset time. The black dashed vertical line denotes the US Geological Survey onset time. The red circle denotes the Mw 7.8 mainshock, blue, yellow, beige circles represent aftershocks of Mw 5.7, Mw 6.7, and Mw 5.6, respectively. The blue circle denotes the Mw 7.5 aftershock, the rose circle—the Mw 6.0 aftershock.

4. Conclusions

In this work, we analyzed ionospheric responses to the series of earthquakes that occurred on 6 February 2023 in Southern Turkey. We separate these events into two groups: the first sequence of earthquakes that occurred at 01–02 UTC and the second sequence that struck at 10–11 UTC.

For the first sequence, we observe a clear N-wave TEC response after the Mw 7.8 mainshock earthquake and to Mw 6.7 aftershock. In addition, we observe a smaller TEC disturbance that is, most likely, due to the Mw 5.6 earthquake, which is now the smallest earthquake detected by using ionospheric GNSS data. The CSID propagated from the epicentral area in the south-west direction with velocities of about 750–830 m/s.

For the second sequence, we observed the response to the Mw 7.5 aftershock earthquake and the Mw. 6.0 aftershock. At first, the CSID propagated both to the south-west and the north-west to the epicentral area, with velocities of about 950–1,100 m/s. During the next 2 min, the CSID was observed only on the south-western from the epicenter.

We note that the CSID velocities and directions of propagation were estimated by using two NRT-compatible techniques that were tested and further improved in the case of the Turkey earthquakes. Besides these NRT-compatible approaches, up to now, only one other method has been developed for the automatic detection of CSID in NRT (Brissaud & Astafyeva, 2022). It uses the Random Forest algorithm and is trained over an extensive ionospheric data set to first classify ionospheric signatures into CSID and noise, and then pick the CSID arrival time.

Data Availability Statement

CDDIS GNSS data are available from the CDDIS data archives (<https://cddis.nasa.gov/archive/gnss/data/daily/>). Turkey GNSS Network data are available from the TUSAGA-Aktif data archives (https://www.tusaga-aktif.gov.tr/DepremVerileri/06022023_KMarasData.rar). The CYPOS data used in this research were kindly provided by the Cyprus Department of Lands and Surveys (<https://portal.dls.moi.gov.cy/en/>).

Ionosonde station AT138 data are available from the DIDBase Web Portal (<https://lgdc.uml.edu/common/DIDBDayStationStatistic?ursiCode=AT138&year=2023&month=2&day=6>).

Data are freely available through the IGP Research Collection (<https://research-collection.ipgp.fr/>) at the following DOI: <https://doi.org/10.18715/IPGP.2023.1ldj6xb9> (TEC and Ionograms data for the 6 February 2023 Türkiye earthquake, 2023; Maletckii et al., 2023).

Figures 2–5 were plotted by using Python (ver. 3.7, libraries “matplotlib.pyplot”: https://matplotlib.org/3.5.0/api/_as_gen/matplotlib.pyplot.html and “cartopy”: <https://scitools.org.uk/cartopy/docs/latest/>). Figure 1 is plotted by the GMT6.0 software that is available at <https://www.generic-mapping-tools.org/download/>.

Acknowledgments

This work was supported by the French National Research Agency (ANR, Grant ANR-22-CE49-0011), by the Fundação de Amparo à Pesquisa do Estado de São Paulo (FAPESP) and by the French Space Agency (CNES, Project “RealDetect”). BM additionally thanks the CNES and the IGP for the Ph.D. fellowship. We thank the Brazilian Ministry of Science, Technology and Innovation and the Brazilian Space Agency. S. A. Sanchez thanks the Coordenação de Aperfeiçoamento de Pessoal de Nível Superior (CAPES) and FAPESP processes 88887.351785/2019-00 and 2023/07807-9, respectively. E. A. Kherani thanks the financial support of the Conselho Nacional de Desenvolvimento Científico e Tecnológico (CNPq) through Grant 307496/2015-5. We acknowledge the use of “tec-suite” codes developed by I. Zhivetiev (<https://tec-suite.readthedocs.io/en/latest/>) and the GMT6.0 software (Wessel et al., 2019). The authors thank L. Rolland and D. T. Mikesell for fruitful discussions, and P. Elliot for his kind help with data from the CYPOS.

References

- Afraimovich, E. L., Feng, D., Kiryushkin, V., & Astafyeva, E. (2010). Near-field TEC response to the main shock of the 2008 Wenchuan earthquake. *Earth Planets and Space*, 62(11), 899–904. <https://doi.org/10.5047/eps.2009.07.002>
- Afraimovich, E. L., Perevalova, N. P., Plotnikov, A. V., & Uralov, A. M. (2001). The shock-acoustic waves generated by the earthquakes. *Annales Geophysicae*, 19(4), 395–409. <https://doi.org/10.5194/angeo-19-395-2001>
- Astafyeva, E. (2019). Ionospheric detection of natural hazards. *Reviews of Geophysics*, 57(4), 1265–1288. <https://doi.org/10.1029/2019RG000668>
- Astafyeva, E., Rolland, L. M., & Sladen, A. (2014). Strike-slip earthquakes can also be detected in the ionosphere. *Earth and Planetary Science Letters*, 405, 180–193. <https://doi.org/10.1016/j.epsl.2014.08.024>
- Astafyeva, E., Shalimov, S., Olshanskaya, E., & Lognonné, P. (2013). Ionospheric response to earthquakes of different magnitudes: Larger quakes perturb the ionosphere stronger and longer. *Geophysical Research Letters*, 40(9), 1675–1681. <https://doi.org/10.1002/grl.50398>
- Bagiya, M. S., Heki, K., & Gahalaut, V. K. (2023). Anisotropy of the near-field coseismic ionospheric perturbation amplitudes reflecting the source process: The 2023 February Turkey earthquakes. *Geophysical Research Letters*, 50, e2023GL103931. <https://doi.org/10.1029/2023gl103931>
- Bagiya, M. S., Sunil, A. S., Rolland, L., Nayak, S., Ponraj, M., Thomas, D., & Ramesh, D. S. (2019). Mapping the impact of non-tectonic forcing mechanisms on GNSS measured coseismic ionospheric perturbations. *Scientific Reports*, 9(1), 18640. <https://doi.org/10.1038/s41598-019-54354-0>
- Bagiya, M. S., Sunil, A. S., Sunil, P. S., Sreejith, K. M., Rolland, L., & Ramesh, D. S. (2017). Efficiency of coseismic ionospheric perturbations in identifying crustal deformation pattern: Case study based on M_w 7.3 May Nepal 2015 earthquake. *Journal of Geophysical Research: Space Physics*, 122(6), 6849–6857. <https://doi.org/10.1002/2017JA024050>
- Bilitza, D., Altadill, D., Truhlik, V., Shubin, V., Galkin, I., Reinisch, B., & Huang, X. (2017). International reference ionosphere 2016: From ionospheric climate to real-time weather predictions. *Space Weather*, 15(2), 418–429. <https://doi.org/10.1002/2016SW001593>
- Brissaud, Q., & Astafyeva, E. (2022). Near-real-time detection of co-seismic ionospheric disturbances using machine learning. *Geophysical Journal International*, 230(3), 2117–2130. <https://doi.org/10.1093/gji/ggac167>
- Cahyadi, M. N., & Heki, K. (2015). Coseismic ionospheric disturbance of the large strike-slip earthquakes in North Sumatra in 2012: Mw dependence of the disturbance amplitudes. *Geophysical Journal International*, 200(1), 1–129. <https://doi.org/10.1093/gji/ggu343>
- Calais, E., & Minster, J. B. (1995). GPS detection of ionospheric perturbations following the January 17, 1994, Northridge earthquake. *Geophysical Research Letters*, 22(9), 1045–1048. <https://doi.org/10.1029/95GL00168>
- CSEM-EMSC. (2023). Retrieved from <https://www.emsc-csem.org/Earthquake/tensors.php?id=1218449&year=2023;INFO>
- Emmert, J. T., Drob, D. P., Picone, J. M., Siskind, D. E., Jones, M., Mlynczak, M. G., et al. (2020). NRLMSISE 2.0: A whole-atmosphere empirical model of temperature and neutral species densities. *Earth and Space Science*, 8(3), e2020EA001321. <https://doi.org/10.1029/2020EA001321>
- Haralambous, H., Guerra, M., Chum, J., Verhulst, T. G., Barta, V., Altadill, D., et al. (2023). Multi-instrument observations of various ionospheric disturbances caused by the 6 February 2023 Turkey earthquake. *Aurea*. <https://doi.org/10.22541/essoar.168500329.97063233/v1>
- Heki, K. (2021). Ionospheric disturbances related to earthquakes. In C. Huang, G. Lu, Y. Zhang, & L. J. Paxton (Eds.), *Ionosphere dynamics and applications*. <https://doi.org/10.1002/9781119815617.ch21>
- Heki, K., & Ping, J. (2005). Directivity and apparent velocity of the coseismic ionospheric disturbances observed with a dense GPS array. *Earth and Planetary Science Letters*, 236(3–4), 845–855. <https://doi.org/10.1016/j.epsl.2005.06.010>
- Kherani, E. A., Lognonné, P., Hébert, H., Rolland, L., Astafyeva, E., Ochipintini, G., et al. (2012). Modelling of the total electronic content and magnetic field anomalies generated by the 2011 Tohoku-oki tsunami and associated acoustic-gravity waves. *Geophysical Journal International*, 191(3), 1049–1066. <https://doi.org/10.1111/j.1365-246X.2012.05617.x>

- Liu, J.-Y., Chen, C. H., Lin, C. H., Tsai, H. F., Chen, C. H., & Kamogawa, M. (2011). Ionospheric disturbances triggered by the 11 March 2011 M9.0 Tohoku earthquake. *Journal of Geophysical Research*, *116*(A6), A06319. <https://doi.org/10.1029/2011JA016761>
- Maletckii, B., & Astafyeva, E. (2021a). Determining spatio-temporal characteristics of Coseismic Travelling Ionospheric Disturbances (CTID) in near real-time. *Scientific Reports*, *11*(1), 20783. <https://doi.org/10.1038/s41598-021-99906-5>
- Maletckii, B., & Astafyeva, E. (2021b). Near-real-time analysis of spatio-temporal characteristics of ionospheric disturbances of different origins. In *Session SA022, AGU Fall Meeting 2021, 13–17 December 2021, Hybrid, New Orleans, USA*.
- Maletckii, B., & Astafyeva, E. (2022). Near-real-time analysis of the ionospheric response to the 15 January 2022 Hunga Tonga-Hunga Ha'apai volcanic eruption. *Journal of Geophysical Research: Space Physics*, *127*(10), e2022JA030735. <https://doi.org/10.1029/2022JA030735>
- Maletckii, B., Astafyeva, E., Sanchez, S. A., Kherani, E. A., & De Paula, E. (2023). TEC and ionograms data for the 6 February 2023 Türkiye earthquake [Dataset]. IPGP Research Collection. <https://doi.org/10.18715/IPGP.2023.LLDJ6XB9>
- Maletckii, B., Yasyukevich, Y., & Vesnin, A. (2020). Wave signatures in total electron content variations: Filtering problems. *Remote Sensing*, *12*(8), 1340. <https://doi.org/10.3390/rs12081340>
- Melgar, D., Taymaz, T., Ganas, A., Crowell, B., Öcalan, T., Kahraman, M., et al. (2023). Sub- and super-shear ruptures during the 2023 Mw 7.8 and Mw 7.6 earthquake doublet in SE Türkiye. *Seismica*, *2*(3). <https://doi.org/10.26443/seismica.v2i3.387>
- Meng, X., Vergados, P., Komjathy, A., & Verkhoglyadova, O. (2019). Upper atmospheric responses to surface disturbances: An observational perspective. *Radio Science*, *54*(11), 1076–1098. <https://doi.org/10.1029/2019RS006858>
- Perevalova, N. P., Sankov, V. A., Astafyeva, E. I., & Zhupityaeva, A. S. (2014). Threshold magnitude for ionospheric response to earthquakes. *Journal of Atmospheric and Solar-Terrestrial Physics*, *108*, 77–90. <https://doi.org/10.1016/j.jastp.2013.12.014>
- Rolland, L. M., Vergnolle, M., Nocquet, J.-M., Sladen, A., Dessa, J.-X., Tavakoli, F., et al. (2013). Discriminating the tectonic and non-tectonic contributions in the ionospheric signature of the 2011, Mw7.1, dip-slip Van earthquake, Eastern Turkey. *Geophysical Research Letters*, *40*(11), 2518–2522. <https://doi.org/10.1002/grl.50544>
- Sanchez, S. A., Kherani, E. A., Astafyeva, E., & de Paula, E. R. (2022). Ionospheric disturbances observed following the Ridgecrest earthquakes of 4 July 2019 in California, USA. *Remote Sensing*, *14*(1), 188. <https://doi.org/10.3390/rs14010188>
- Vesnin, A., Yasyukevich, Y., Perevalova, N., & Şentürk, E. (2023). Ionospheric response to the 6 February 2023 Turkey-Syria earthquake. *Remote Sensing*, *15*(9), 2336. <https://doi.org/10.3390/rs15092336>
- Wessel, P., Luis, J. F., Uieda, L., Scharroo, R., Wobbe, F., Smith, W. H. F., & Tian, D. (2019). The generic mapping tools version 6. *Geochemistry, Geophysics, Geosystems*, *20*(11), 5556–5564. <https://doi.org/10.1029/2019GC000851>